Full-potential linearized augmented plane-wave method for one-dimensional systems: Gold nanowire and iron monowires in a gold tube

Y. Mokrousov,* G. Bihlmayer, and S. Blügel
Institut für Festkörperforschung, Forschungszentrum Jülich, D-52425 Jülich, Germany
(Received 10 February 2005; published 1 July 2005)

We present an implementation of the full-potential linearized augmented plane-wave (FLAPW) method for carrying out *ab initio* calculations of the ground state electronic properties of (magnetic) metallic nanowires and nanotubes based on the density-functional theory (DFT). The method is truly one-dimensional, uses explicitly a wire geometry and is realized as an extension of the FLEUR code. It includes a wide variety of chiral symmetries known for tubular and other one-dimensional systems. A comparative study shows that in this geometry computations are considerably faster than the widely used supercell approach. The method was applied to some typical model structures explored in the field of nanospintronics: the gold nanowire Au(6,0), the free-standing Fe monowire, and the hybrid structure Fe@Au(6,0). Their atomic structures are determined by total energy minimization and force calculations. We calculated the magnetic properties including the magnetocrystalline anisotropy energies, the band structures, and densities of states in these systems using the local density approximation (LDA) and the generalized gradient approximation (GGA) to the DFT. The results agree nicely with the data available in the literature. We found that Fe wires are ferromagnetic and are prone to a Peierls dimerization. The Fe filled gold nanotube shows a large negative spin polarization at the Fermi level, which makes this structure a possible candidate for spin-dependent transport applications in the field of spintronics. The Au tube encasing the Fe wire changes the magnetization direction of the Fe wire and increases the magnetocrystalline anisotropy energy by an order of magnitude.

DOI: 10.1103/PhysRevB.72.045402 PACS number(s): 73.63.Fg, 73.63.Nm, 72.25.−b, 71.15.Ap

I. INTRODUCTION

In recent years we witnessed enormous progress in the chemical synthesis, growth, and the development of technology allowing the fabrication of a rich variety of nanomaterials with unprecedented properties. As the scale of nanomaterials continue to decrease from the mesoscopic regime to the atomic scale, one-dimensional (1D) nanometer scale systems such as carbon nanotubes,[1] radially and axially modulated semiconductor nanowires,[2] and thin metallic quantum wires[3–5] moved into the focus of attention. The excitement in these one-dimensional structures is fueled by their wealth of new physical phenomena such as quantized conductance, charge and spin separation, intriguing structural and magnetic properties such as high spin-polarization and large spin-scattering lengths.[6]

They are also important from a technological point of view. For example, the ability to fabricate thin metallic interconnects with favorable properties is an important factor determining the progress of ultralarge scale integrated circuits. In many cases the transport properties of these systems can be easily tuned by choosing suitable structural parameters such as the diameter or chirality. Moreover, the diameters of many experimentally observed 1D structures are much smaller than most semiconductor devices obtained so far, and thus one can imagine that the smallest possible transistors are likely to be based on them.[7–9]

Today a large variety of one-dimensional structures are known and continue to be synthesized. First and foremost are the single walled (SWNT) and multiwalled (MWNT) one-dimensional tubular structures, which exist not only for carbon, but also for GaN,[10] BN,[11] TiO,[12] VO,[13] and other compounds. A further large class are the quasi-1D crystals, a family of structures with different diameters and chiralities, chemical, and physical properties.[14] They involve elements from the entire Periodic Table. In the context of magnetoelectronics and spintronics we witness two important trends in the synthesis of one-dimensional magnetic hybrid structures. One is based on the development of new nanotube production technologies which allow one to fill for example carbon nanotubes[15,16] and other nanotubes with metals.[17] The other one rests in the field of organometallics. Molecular magnets with a tendency towards one-dimensionalization are synthesized and experimentally observed as quasi-1D structures showing intriguing magnetic and structural properties.[18,19]

In order to understand the structure-property relation in these new materials on the basis of the electronic structure, *ab initio* calculations based on the density functional theory play an important role. The low-dimensionality, the chemical complexity, the open structure, and the large variety of chemical elements in these systems ask for flexible *ab initio* methods, which can cope with these issues. Methods employed for density-functional calculations of one-dimensional systems include the tight-binding,[20] pseudopotential,[21] linearized muffin-tin orbital LMTO,[22] and the PAW (Ref. 23) and FLAPW (Refs. 24 and 25) supercell formalism. Although applicable to a range of materials, the first two methods are usually not optimal for a highly precise description of the electronic properties of low-dimensional systems containing, for instance, (magnetic) transition elements. From this point of view FLAPW would be an optimal calculating scheme, although, as for the pseudopotential and PAW method, one-dimensional structures are treated in the

supercell geometry, i.e. in a two-dimensional lattice of one-dimensional structures. Obviously, either one has to deal with very large supercells or one has to accept a degree of interactions coming from the neighboring unit cells at finite distance. Further, in the supercell geometry the symmetries characteristic for the 1D systems are not naturally included.

In this paper we present an efficient and very precise all-electron method for carrying out *ab initio* calculations based on density functional theory of electronic ground state properties for systems having a one-dimensional periodicity, in particular, metallic wires and nanotubes. The method is truly one-dimensional, i.e. it is applied for calculations of single wires or tubes surrounded by infinite vacuum, avoiding any interaction due to the presence of the neighboring unit-cells. The truly one-dimensional structure model can lead to a large computational speed-up over the conventional supercell approach opening opportunities to study more complex systems. Including the symmetries allows us to achieve a further significant speed-up, increased accuracy as well as a simplified analysis of the results.

This approach, which makes use of the chiral symmetries for a considered system, allows us to carry out calculations of the total energies, forces and atomic relaxations, band structures, and densities of states including spin-orbit coupling effects. A particular emphasis was put on the investigation of magnetic properties such as the spin and orbital moment, magnetization direction, and the magnetic structure.

In further developing the opportunities of one-dimensional hybrid structures we investigate the electronic properties, geometrical and magnetic structure of a Au(6,0) and an Fe@Au(6,0) nanowire. In addition we perform first-principles calculations for a Au(6,0) nanotube, and freestanding Au and Fe monowires. The results show, that the bare Fe monowire and the Fe monowire inside the Au(6,0) are ferromagnetic. The Au coverage of the Fe monowire causes a change of the easy magnetization axis, which is along the wire for the single Fe monowire and perpendicular to the wire for the Au covered Fe wire. This is in part explained by the large spin-orbit interaction of Au. The Fe@Au(6,0) hybrid structure exhibits a large negative spin polarization at the Fermi energy, which makes this system interesting as a potential candidate for spin-dependent transport applications. In this work we focus primarily on straight and linear wires. The investigation of the equilibrium structure based on total energy minimization shows that this system is prone to a Peierls dimerization or zig-zag relaxation. Wires attached to leads experience a string tension[5,25] which alters the atom positions in the wire, an aspect not considered in this paper.

The paper is organized as follows: In Sec. II an overview of the one-dimensional FLAPW method is presented. This includes the definition of the one-dimensional symmetry, the LAPW basis function, charge density, and potential representation in different regions of space. Details are given in respective appendices. Computational parameters and numerical details are explained. Section III results, including the atomic and electronic structure, magnetic properties and the charge density, of the Au(6,0) nanowire and the Fe@Au(6,0) hybrid structure are presented and discussed. The paper is concluded in Sec. IV.

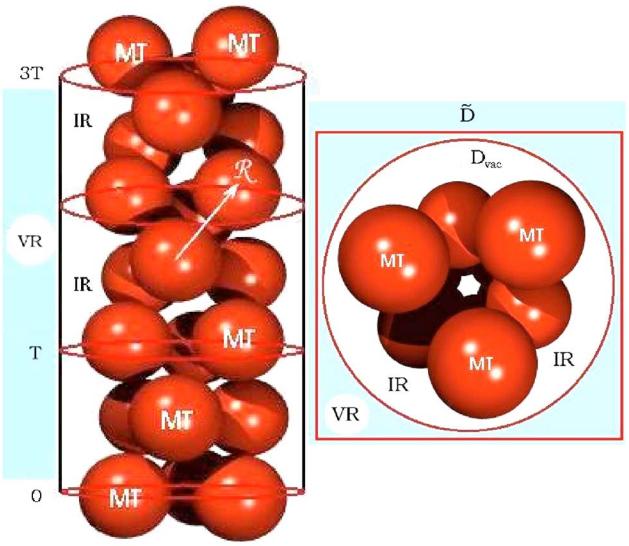

FIG. 1. (Color online) Spatial partitioning of space into muffin-tin spheres (MT), interstitial region (IR), and vacuum region (VR) (shown in blue color) is shown from aside (left) and from the top (right). The vacuum region is the infinite region outside the cylinder with the diameter D_{vac}. T is a period of the wire along the z-axis. $\mathcal{R}=(R_\psi,\tau)$ is a generator of the symmetry group. Here: the order of the group is $N=6$, and $\psi=\frac{\pi}{3}, \tau=\frac{1}{2}$.

II. METHOD

A. Geometry and symmetries

In the proposed FLAPW method for one-dimensional systems, the infinite three-dimensional space is partitioned into three regions: (i) the muffin-tin spheres (MT) with the radius R_{MT} around the atoms, (ii) the interstitial region (IR) between the atoms and within a cylinder along the axis of the wire (z) of the radius R_{vac}, (iii) an infinitely extended vacuum region (VR) outside this cylinder (see Fig. 1). From here on we define the z-axis as the axis of one-dimensional translational symmetry. As our method is based on the use of LAPW basis functions,[26–28] the set of reciprocal vectors $\mathbf{G}=(\mathbf{G}_\parallel, G_z)$ defining the plane-waves is generated in a rectangular box, which reflects the translational periodicity of the system in z-direction. The corresponding Bloch number, k_z, lies within the first one-dimensional Brillouin zone. The in-plane reciprocal lattice vectors $\mathbf{G}_\parallel$ are generated in an in-plane square lattice with the lattice constant $\tilde{D}$. The vacuum region is an infinite region outside the cylinder with the diameter $D_{\mathrm{vac}}<\tilde{D}$ $(D_{\mathrm{vac}}=2R_{\mathrm{vac}})$, with the axis along the z-direction.

The symmetry properties are formulated and included in terms of the chiral symmetry group of the considered system. This means, that the symmetry group $\mathcal{T}$ is cyclic of order N with a generator $\mathcal{R}$ so that for every operation $n=1,\ldots,N: \mathcal{R}_n=\mathcal{R}^n, \mathcal{T}=\{\mathcal{I},\mathcal{R},\ldots,\mathcal{R}_{N-1}\}$. In a three-dimensional space the operation $\mathcal{R}$ is a simultaneous rotation around the z-axis, R_ψ, and a translation along the z-axis, τ, i.e. $\mathcal{R}=(R_\psi,\tau)$. Obviously, $\psi=2\pi/N$, and $\tau=(M\cdot T)/N$, where M is some integer number and T is a period of the system along the z-direction.

Let us consider the example of a wire obtained by rolling up a sheet of atoms, having a triangular lattice (for details see Refs. 5 and 29 with the chiral vector $\mathbf{C}_h=(m,n)$ in units of the two-dimensional basis vectors $\mathbf{a}_1,\mathbf{a}_2$: the planar representation of a symmetry group generator $\mathbf{R}=(p,q)$ is a lattice vector having the smallest projection on $\mathbf{C}_h$, and the number of symmetry operations $N=[2(m^2+n^2-nm)]/d_R$ is equal to the number of atoms in the unit cell, where d_R is a greatest common divisor of $(2m-n)$ and $(m-2n)$. Then, the translational part of $\mathcal{R}$ is given by $\tau=[(mp-nq)T]/N$, with $M=mp-nq$. For example, for the (6,0) wire (see Fig. 2) $\mathbf{R}$ would be (1,1), $d_R=6$, $N=12$, $M=6$, $\psi=\pi/6$, and $\tau=\frac{1}{2}$ in units of T.

In Fig. 1 we have shown a (6,3) nanowire obtained by rolling a triangular sheet of atoms with $\mathbf{C}_h=(6,3)$. In this case $\mathbf{R}=(1,1)$, and $d_R=9$, $N=6$, $M=3$, $\psi=\pi/3$, and $\tau=\frac{1}{2}$ in units of T.

B. FLAPW formalism

1. Basis functions

As characteristic for the FLAPW method, optimally adjusted basis functions are used in the three different regions of space:

$$\varphi_{\mathbf{G}}(k_z,\mathbf{r})=\begin{cases} e^{i(\mathbf{G}+k_z)\mathbf{r}} & \text{in IR} \\ \sum_L (A_L^{\alpha\mathbf{G}}(k_z)u_l^\alpha(r)+B_L^{\alpha\mathbf{G}}(k_z)\dot{u}_l^\alpha(r))Y_L(\hat{\mathbf{r}}) & \text{in MT}^\alpha \\ \sum_m (A_m^{\mathbf{G}}(k_z)u_m^{G_z}(k_z,r)+B_m^{\mathbf{G}}(k_z)\dot{u}_m^{G_z}(k_z,r))e^{im\varphi}e^{i(G_z+k_z)z} & \text{in VR.} \end{cases} \quad (1)$$

In the interstitial region the basis functions $\varphi_{\mathbf{G}}(k_z,\mathbf{r})$ are usual plane-waves with the Bloch vector $\mathbf{k}=(0,0,k_z)$.

In the sphere MT$^\alpha$ the basis functions for each atom α have the well-known form of products of spherical harmonics $Y_L(\hat{\mathbf{r}}),L=(l,m)$, and of the radial wave functions $u_l^\alpha(r)$ and their energy derivatives $\dot{u}_l^\alpha(r)$. These are radial solutions of Schrödinger-type scalar-relativistic equations, which are solved for each angular momentum $l\leqslant l_{\max}$, for the spherical part of the potential $V_0^{\mathrm{MT}^\alpha}(r)$ and suitably chosen energy parameters E_l.[30]

In the vacuum region the space coordinate $\mathbf{r}$ is written in terms of cylindrical coordinates (r,φ,z). The summation over m goes up to the angular expansion parameter $m_{\max}$, which ensures that the oscillations of the plane-waves on the cylindrical vacuum boundary continue smoothly to the vacuum side. Since the vacuum potential is rather flat, relativistic effects on the basis functions can safely be ignored. Thus the cylindrically symmetrical part of the vacuum potential $V_0(r)$ and the vacuum energy parameter E_v, determined in every iteration, enter the radial Schrödinger equation, which is solved for every pair (m,G_z) giving rise to the vacuum radial basis wave functions $u_m^{G_z}(k_z,r)$ and their energy derivatives $\dot{u}_m^{G_z}(k_z,r)$.

The sets of augmentation coefficients A and B both for the MT spheres and the vacuum region are determined such that the basis functions and their spatial derivatives are continuous across the MT spheres, interstitial and vacuum region boundaries. The equations and normalization conditions for the radial functions $u_m^{G_z}(k_z,r)$ and $\dot{u}_m^{G_z}(k_z,r)$, and expressions for A and B coefficients are given in Appendix A.

All the basis functions with reciprocal lattice vector $\mathbf{G}$ that fulfill the condition $|k_z+\mathbf{G}|<K_{\max}$ are included. The corresponding representation of the charge density and potential involves all vectors $\mathbf{G}$ with $|\mathbf{G}|<G_{\max}$. Typically, we choose $G_{\max}\approx 3\cdot K_{\max}$, in order to describe properly the multiplication of the interstitial potential with the step function using fast Fourier transformations. The vacuum angular parameter $m_{\max}$ is defined in the same manner as $l_{\max}$ in the spheres,[30] $m_{\max}\simeq K_{\max}\cdot R_{\mathrm{vac}}$.

In the case of carrying out spin-polarized calculations for magnetic systems, the basis functions, and all the matrix elements discussed below, carry an additional spin index $\sigma=\uparrow,\downarrow$, which is dropped here for simplicity.

2. Eigenvalue problem

The wave function $\Psi_{k_z}^\nu(\mathbf{r})$ for a certain k_z-point and an energy band ν is expanded in terms of basis functions as

$$\Psi_{k_z}^\nu(\mathbf{r})=\sum_{\mathbf{G}} c_\nu^{\mathbf{G}}(k_z)\varphi_{\mathbf{G}}(k_z,\mathbf{r}), \quad (2)$$

where the expansion coefficients $c_\nu^{\mathbf{G}}(k_z)$ and the corresponding eigenvalues $\epsilon_\nu(k_z)$ are found by minimizing the Rayleigh-Ritz functional,

$$\epsilon_\nu(k_z)=\frac{\langle\Psi_{k_z}^\nu|\mathcal{H}|\Psi_{k_z}^\nu\rangle}{\langle\Psi_{k_z}^\nu|\Psi_{k_z}^\nu\rangle} \quad (3)$$

with respect to the expansion coefficients. $\mathcal{H}$ is the Hamiltonian of the system. Minimization of Eq. (3) leads to the generalized eigenvalue problem:

$$\{\mathbf{H}(k_z)-\epsilon_\nu(k_z)\mathbf{S}(k_z)\}c_\nu^{\mathbf{G}}(k_z)=0, \quad (4)$$

where the appearance of the overlap matrix $\mathbf{S}(k_z)$ is due to the nonorthogonality of basis functions. The elements of the

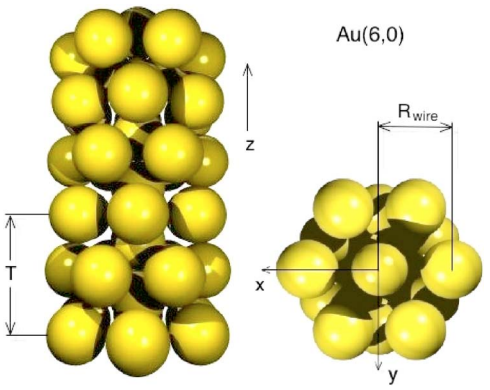

FIG. 2. (Color online) Geometrical structure of a Au(6,0) nanowire. Left: side view. Right: top view. The unit cell contains 12 atoms in the outer shell and 2 atoms in the central strand.

Hamiltonian and overlap matrices are given by following expressions:

$$H^{\mathbf{G}'\mathbf{G}}(k_z) = \int \varphi^*_{\mathbf{G}'}(k_z,\mathbf{r})\mathcal{H}\varphi_{\mathbf{G}}(k_z,\mathbf{r})d^3r, \tag{5}$$

$$S^{\mathbf{G}'\mathbf{G}}(k_z) = \int \varphi^*_{\mathbf{G}'}(k_z,\mathbf{r})\varphi_{\mathbf{G}}(k_z,\mathbf{r})d^3r. \tag{6}$$

The integration goes over the entire unit cell. Analytic expressions for the matrix elements are given in Appendix B.

3. Charge density

The charge density is represented according to the symmetries of the system in the following way:

$$\rho(\mathbf{r}) = \begin{cases} \sum_{\mathbf{G}} \rho_{\mathbf{G}} e^{i\mathbf{G}\mathbf{r}} & \text{in IR} \\ \sum_{\nu} \rho_{\nu}(r_\alpha) K_\nu(\hat{\mathbf{r}}_\alpha) - Z_\alpha \delta(\mathbf{r}_\alpha) & \text{in MT}^\alpha \\ \sum_{\mu} \rho_\mu(r)\Phi_\mu(\varphi,z) & \text{in VR} \end{cases} \tag{7}$$

where

$$K_\nu(\hat{\mathbf{r}}) = \sum_m c_m(\nu) Y_{l_\nu m}(\hat{\mathbf{r}}) \tag{8}$$

are the lattice harmonics, obtained by exploiting the point symmetry of the atom α, and $\mathbf{r}_\alpha = \mathbf{r} - \boldsymbol{\zeta}_\alpha$. Here $\boldsymbol{\zeta}_\alpha$ is the position of the atomic sphere α with the nuclear number Z_α. The quantities in the spheres, like radial components of the charge density, potential, and basis functions are calculated and stored only for the representative atom of type α. All necessary information on the charge density of an equivalent atom β, which is related by symmetry to the atom α can then be obtained exploiting the fact that the local coordinate frame of the atom β, $\mathcal{S}_\beta$, is related to the coordinate frame $\mathcal{S}_\alpha$ by the symmetry operation $\mathcal{R}_{\beta(\alpha)}$ which moves the representative atom α to the βth atom of the same type $\mathcal{S}_\beta = \mathcal{R}_{\beta(\alpha)}\mathcal{S}_\alpha$.

In the vacuum, symmetry can be used to reduce the number of expansion coefficients, necessary to represent the charge density by introducing star functions. For a certain $\mu = (m, G_z)$ a vacuum symmetrized two-dimensional star $\Phi_\mu(\varphi,z)$ looks like

$$\Phi_\mu(\varphi,z) = \frac{1}{N}\sum_{n=1}^{N} \mathcal{R}_n e^{im\varphi} e^{iG_z z}. \tag{9}$$

We keep those μ for which $\rho_\mu(r) \neq 0, r \geq R_{\text{vac}}$. For instance, having a rotational symmetry of order p reduces the number of μ's to consider by a factor p. The summation in Eq. (7) includes μ's with m's up to a parameter $m_{\max}$, defined for the charge density in the vacuum as $m_{\max} \approx G_{\max} \cdot R_{\text{vac}}$, in analogy to the corresponding angular expansion parameter for the basis functions in the vacuum.

In the interstitial region a double representation of the charge density is used

$$\rho(\mathbf{r}) = \sum_{\mathbf{G}} \rho_{\mathbf{G}} e^{i\mathbf{G}\mathbf{r}} \leftrightarrow \sum_{\mathbf{G}} \rho_{\mathbf{G}} \Phi_{\mathbf{G}}(\mathbf{r}), \tag{10}$$

where $\Phi_{\mathbf{G}}(\mathbf{r})$ is a symmetrized three-dimensional star,

$$\Phi_{\mathbf{G}}(\mathbf{r}) = \frac{1}{N}\sum_{n=1}^{N} \mathcal{R}_n e^{i\mathbf{G}\mathbf{r}} = \frac{1}{N}\sum_{n=1}^{N} e^{iR_n\mathbf{G}(\mathbf{r}-\tau_n)}. \tag{11}$$

The necessity of the double representation is caused by the nonorthogonality of the symmetrized stars $\Phi_{\mathbf{G}}$. This means, that in contrast to the standard situation of dealing with usual plane-waves, the integral of a symmetrized star $\Phi_{\mathbf{G}}(\mathbf{r})$ over the tetragonal unit cell with the in-plane lattice constant $\tilde{D}$ is not necessarily zero for $\mathbf{G} \neq 0$. Also, the product of two symmetrized stars is not a symmetrized star, which means, that it cannot be presented in the form of Eq. (11) anymore (although, being a symmetrical function, it can be expanded in terms of symmetrized stars). The combination of the latter two facts makes the application of the fast Fourier transformation (FFT) technique, widely used in plane-wave based codes, difficult.

For the potential we use the same representation as for the charge density in Eq. (7), also dividing the space into three different regions.

After finding the expansion coefficients $c_\nu^{\mathbf{G}}(k_z)$, the eigenvalues $\epsilon_\nu(k_z)$, and the Fermi energy E_F, the charge density is determined as

$$\rho(\mathbf{r}) = \sum_{k_z}\sum_{\nu} w(k_z) f(\nu,k_z) |\Psi^\nu_{k_z}(\mathbf{r})|^2, \tag{12}$$

where the summation goes over the one-dimensional Brillouin zone with the weighting factors $w(k_z)$ and the Fermi function $f(\nu,k_z)$. The expression for the charge density in the vacuum in terms of the A,B-coefficients and the radial basis functions is given in Appendix A.

4. Coulomb potential

The potential used for solving the one-particle Kohn-Sham equation is divided into the Coulomb and exchange correlation parts. While the latter is obtained on a real-space grid in a quite straightforward manner, the Coulomb potential requires more attention.

Conceptually, the approach for solving the Poisson equation goes back to Weinert's pseudocharge scheme for the Dirichlet problem[31] for the spheres and vacuum boundaries. The basic idea of the pseudocharge scheme is that the charge distributions inside the spheres contribute to the potential outside the spheres only via their multipole moments. As multipole moments do not uniquely define a charge density, we replace the real charge density in the spheres by a so-called pseudocharge density with the same multipole moments fulfilling the additional requirement of having rapidly converging Fourier components. These Fourier components together with the vacuum charge density take part in solving the Poisson equation in the vacuum. After that the Dirichlet problem for the interstitial-vacuum boundary is solved in order to find the Fourier components of the interstitial potential. Subsequently, the Coulomb potential in the spheres is found via the interstitial-spherical Dirichlet boundary problem,

$$V_\alpha(\mathbf{r}_\alpha) = \int_{S_\alpha} \rho_\alpha(\mathbf{r}) G(\mathbf{r},\mathbf{r}_\alpha) d^3r - \frac{R_\alpha^2}{4\pi} \oint_{S_\alpha} V_I(\mathbf{R}_\alpha) \frac{\partial G}{\partial n} d\Omega, \tag{13}$$

where S_α denotes a sphere around atom α with the radius R_α, $\mathbf{R}_\alpha$ is a point on ∂S_α, V_I is the interstitial potential, and the Green function $G(\mathbf{r},\mathbf{r}_\alpha)$ and its normal derivative are given in Ref. 31.

The Poisson equation in the vacuum is solved in cylindrical coordinates using the boundary condition at infinity,

$$\lim_{r\to\infty} V(r) = 0, \quad \lim_{r\to\infty} \frac{\partial V(r)}{\partial r} = 0. \tag{14}$$

Thus, we introduce the zero energy as an absolute reference from which all energies are measured. For example, the work function is then just given by the negative of the Fermi energy E_F. The radial Poisson equation which describes the (m,G_z)-component of the vacuum potential in cylindrical coordinates is given by

$$\left(\frac{d^2}{dr^2} + \frac{1}{r}\frac{d}{dr} - G_z^2 - \frac{m^2}{r^2}\right) V_{G_z,m}(r) = -4\pi\rho_{G_z,m}(r). \tag{15}$$

The equation is solved using the Green function G_{m,G_z}, which satisfies above defined boundary conditions:

$$G_{m,G_z}(r,r') = \begin{cases} -4\pi \ln r_< & m = G_z = 0 \\ \dfrac{2\pi}{m}(r_</r_>)^m & G_z = 0, m \neq 0 \\ 4\pi I_m^{G_z}(r_<) K_m^{G_z}(r_>) & m \cdot G_z \neq 0 \end{cases} \tag{16}$$

where $r_> = \max(r,r')$, $r_< = \min(r,r')$, $I_m^{G_z}$ and $K_m^{G_z}$ are the modified cylindrical Bessel and MacDonald functions I_m and K_m of order m: $I_m^{G_z}(r) = I_m(G_z r)$, $K_m^{G_z}(r) = K_m(G_z r)$. The radial component of the Coulomb potential in the vacuum $V_\mu^V(\mathbf{r})$ is obtained in terms of the radial charge density as

$$V_{G_z,m}^V(r) = \int_0^\infty r' G_{m,G_z}(r,r') \rho_{G_z,m}(r') dr', \quad r > R_{\text{vac}}. \tag{17}$$

Note, that the integration ranges between $0 \leqslant r' \leqslant R_{\text{vac}}$. Thus it includes the interstitial region, where the charge density has a three-dimensional Fourier representation. The corresponding radial components of the interstitial charge density read

$$\rho_{G_z,m}(r) = \sum_{\mathbf{G}_\parallel} i^m \rho_{G_z,\mathbf{G}_\parallel} e^{-im\varphi_{\mathbf{G}_\parallel}} J_m(G_\parallel r), \tag{18}$$

with J_m denoting the cylindrical Bessel functions of order m and $\varphi_{\mathbf{G}_\parallel}$ is the polar coordinate of the in-plane component $\mathbf{G}_\parallel$ of a reciprocal vector. Therefore, the integration over the interstitial region is reduced to a $\mathbf{G}_\parallel$-summation on the vacuum boundary for each (m,G_z)-component. On the interstitial-vacuum boundary a value of the vacuum potential V_b^V is obtained.

In the next step we construct the potential $\tilde{V}$ in the interstitial region, having following Fourier components:

$$\tilde{V}_{\mathbf{G}} = \frac{4\pi}{G^2}\rho_{\mathbf{G}}, \quad \text{and } \tilde{V}_{\mathbf{0}} = 0, \tag{19}$$

with the interstitial-vacuum boundary value $\tilde{V}_b$. Applying a FFT to $\tilde{V}$ we get it on a real grid in the interstitial. The second auxiliary interstitial potential $\mathcal{V}$ we use solves the boundary problem:

$$\Delta\mathcal{V}(\mathbf{r}) = 0, \quad r \in \text{IR}, \quad \mathcal{V}_\text{b} = V_\text{b}^V - \tilde{V}_\text{b}, \tag{20}$$

where $\mathcal{V}_\text{b}$ is a boundary value of $\mathcal{V}$. This potential is easily found analytically on the real grid. After the real grid summation and applying backward FFT to $\tilde{V}+\mathcal{V}$ we get the Fourier components of the real interstitial potential $V_I(\mathbf{G})$.

C. Computational aspects

1. Vacuum parameters

The idea of introducing the vacuum region as a separate semi-infinite cylindrical region of space for one-dimensional calculations is—to our knowledge—new in the APW-family of methods, and here we would like to present some typical numerical values for the parameters we usually use in the calculations.

The $u_m^{G_z}(k_z,r)$ and $\dot{u}_m^{G_z}(k_z,r)$ basis functions as well as the charge density and potential in the vacuum region are represented on an equidistant radial grid. Experience has shown that a grid spacing of $dr = 0.08$ a.u. and the assumption that the unperturbed vacuum is reached after 250 points, leads to numerically converged results. Similar values (grid spacing $dr = 0.1$ a.u. and 250 grid points) have been used for the vacuum in the film-FLAPW (Ref. 27) method to embed truly 2D periodic systems in semi-infinite vacua.

The parameter $\Delta D = \tilde{D} - D_{\text{vac}}$ in the range of $R_{\text{MT}} \pm 0.5$ a.u. enables precise and stable calculated quantities.

The choice of the angular expansion parameter $m_{\max}$ for the basis functions should be around one-half of the corresponding angular parameter for the charge density and the potential.

2. Exchange correlation potential in the vacuum

As we have already mentioned, the exchange correlation potential $V_{\mathrm{xc}}(\mathbf{r})$ in the vacuum region, as well as in the interstitial and MT regions, is determined on the real space grid in cylindrical coordinates (r,φ,z). For a given radial point r_i in the vacuum the two-dimensional charge density $\rho(r_i;\varphi,z)$ is evaluated with a two-dimensional FFT. This means, that $\rho(r_i;\varphi,z)$ and the two-dimensional exchange correlation potential $V_{\mathrm{xc}}(r_i;\varphi,z)$ [as a function of the charge density $\rho(r_i;\varphi,z)$] are found on a discrete equidistant grid in the (φ,z) plane $\{\varphi,z:0\leqslant\varphi<2\pi,0\leqslant z<T\}$. Further, the back Fourier transformation in this plane gives us a set of Fourier coefficients $\{V_{\mathrm{xc},\mu}(r_i)\}$—the coefficients of the two-dimensional stars $\Phi_\mu(\varphi,z)$ in the expansion of the exchange correlation potential [see Eq. (7)]. This is repeated for all radial grid points r_i points. At the end of the procedure, the exchange correlation potential is added to the Coulomb potential on the radial grid.

In the case of GGA the exchange correlation potential also depends on the spatial gradients of the charge density, which are calculated in the vacuum region in cylindrical coordinates (expressions for these gradients can be found in Appendix C).

Having an equidistant angular grid on the segment $(0, 2\pi)$ with a fixed number of points given by $m_{\max}$, causes obviously an increase in the distance between the grid points in absolute proportionally to r_i. Therefore, it might seem that the accuracy in the description of the exchange correlation potential (and the charge density) decreases as r_i increases. But actually the accuracy of the representation is only determined by $m_{\max}$, assuming to be the same for every r_i. Furthermore, the exchange correlation potential decays very fast into the vacuum. Therefore, beyond a certain radial point r_0, which may be reached at about 10 a.u. from R_{vac}, only the cylindrically symmetric component of the potential becomes really important. In a similar spirit, in the film-FLAPW method,[27] for the last 150 grid points of the vacuum, only the z-dependent part of the potential can be kept.

3. Timing

In order to give the reader an impression about the computational cost for computing the vacuum region we have analyzed the timing of the Hamiltonian and overlap matrix setup, the charge density and potential generation. The timing was measured for a bare Au(6,0) tube with 12 atoms per unit cell with the computational parameters as described in Sec. III A. The set-up of the Hamiltonian and overlap matrices for the vacuum region takes about 10% of the overall time spent to set up these matrices, which amounts to 2.5% of the entire time to solve the eigenvalue problem including the diagonalization. The construction of the vacuum charge density takes 0.9% of the total time per iteration and a fraction of 2% of the total time per self-consistency iteration is spent for the generation of the vacuum potential (including Coulomb and exchange correlation potential within the LDA). In total, for a 12 atom Au(6,0) tube the total time spent for calculating the vacuum region amounts to 5% of the entire CPU time for one iteration with 11 k-points in one half of the Brillouin zone.

We have also performed comparative calculations of a gold monowire, once calculated with the 1D code presented in this paper as well as with a bulk code, whereas for the latter a wide variety of methods are readily available applying a frequently practiced supercell approach to simulate the 1D geometry. In order to provide an interpretable comparison, we have used the same computer hardware and for the supercell calculations also the FLAPW bulk method as implemented in the FLEUR code. In both approaches we have exploited the following symmetry elements: inversion, z-reflection and $p4m$ symmetry group. For the truly one-dimensional calculations we have chosen for the computational parameters D_{vac} and $\tilde{D}$ the values of 4.8 a.u. and 5.9 a.u., respectively. The angular expansion parameter $m_{\max}=50$ for the charge density and potential, and 20 for the basis functions proved to provide the required accuracy. To simulate the 1D wires in the supercell approach, we followed the work of Delin and Tosatti[24] in choosing the geometrical set-up. Thus, we used a tetragonal supercell and the distance between the neighboring monowires was set to 19 a.u. For the calculations we used 64 k-points in one half of the Brillouin zone. The rest of the parameters were the same for both calculations. We found that per self-consistency iteration the 1D-method is about 150 times faster than the supercell approach, and the Hamiltonian construction and the diagonalization part of the 1D code is about 270 times faster than that of the bulk supercell code.

For completeness we compare also the timing with the supercell approach using the film geometry[27] (a truly two-dimensional method with semi-infinite vacuum on both sides of a slab of a finite thickness), also implemented in the FLEUR code. In this supercell geometry the one-dimensional wires are simulated by a two-dimensional rectangular unit cell where the wires are again separated by 19 a.u. The parameters D_{vac} and $\tilde{D}$ were set to 4.8 a.u. and 5.9 a.u., respectively. All other computational parameters where chosen as in the bulk and 1D-geometry. We found that per self-consistency iteration the 1D-method is 15 times faster than this supercell approach with 64 k-points in one half of the Brillouin zone, and the Hamiltonian construction and the diagonalization part of the 1D code is 25 times faster than that of the film supercell code.

Finally, we would like to mention, that the code was parallelized for CRAY T3E and IBM SP4 supercomputers.

III. RESULTS AND DISCUSSION

A. Gold nanowire Au(6,0)

Frequently metallic wires are produced by forming a break junction, i.e., by pulling off two pieces of material. During this process a one-dimensional bridge appears, which then elongates, narrows and breaks. Experimentally such

bridges were formed for Au,[32] Pt,[33] and Ir.[34] With respect to the bulk materials these free-standing nanowires are of course unstable, but when some "magic geometries" are reached, wires with lengths of about 15 nm and long lifetimes were reported. Structurally more stable metallic nanowires can form on stepped surfaces or inside tubular structures.

Recently, several experimental[3,29,35] and theoretical[5,24,36] studies have been published on structural and physical properties of different gold nanowires. Here, we want to report on calculations of a Au(6,0) nanowire with our new code. For the illustrative purposes we also perform calculations of a Au(6,0) nanotube and a Au monowire, and compare the obtained results with those available in the literature.

1. Computational details

GGA and LDA calculations are carried out using values of 3.6 a.u.$^{-1}$ and 10.8 a.u.$^{-1}$ for the cut-off parameters $K_{\max}$ and $G_{\max}$, respectively. For the GGA calculations we used the revPBE functional[37] and the Vosko, Wilk, and Nusair functional[38] was applied for the LDA calculations. The muffin-tin radii for the gold atoms were fixed at 2.0 a.u. during the calculations. For the basis functions as well as the charge density and potential in the vacuum region we used the angular expansion parameters $m_{\max}=24$ and $m_{\max}=50$, respectively. The vacuum parameters $D_{\text{vac}}=15.0$ a.u. and $\tilde{D}=16.6$ a.u., and a grid spacing $dr=0.08$ a.u. and 250 grid points for the representation of all real space quantities in the vacuum region were sufficient to reach the required numerical accuracy. Structural optimization was done using 11 k-points in one half of the Brillouin zone, the band structures and densities of states were calculated using 41 k-points in one half of the Brillouin zone. The Au(6,0) nanotube and the free-standing Au MW were calculated with the same computational parameters.

2. Geometrical structure

The structure of the wire, having 14 gold atoms in the unit cell, is shown in Fig. 2. It consists of a central strand of Au atoms and an outer shell Au(6,0) tube. Every atom of the central MW was placed in between the planes of outer hexagons along the symmetry axis of the nanowire. We did not consider the possibility of dimerization or creation of zig-zag structures for the inner Au MW inside the Au(6,0) tube.

Within the GGA we found an optimized period T in z-direction of 8.84 a.u. and a wire radius R_{wire} of 5.21 a.u. (the wire radius, R_{wire}, is defined in Fig. 2), while the LDA calculations led to the optimized T value and wire radius of 8.86 a.u. and 5.16 a.u., respectively. This is in a good agreement with Ref. 5, where $R_{\text{wire}}\approx 5.3$ a.u. and $T=8.82$ a.u. have been found. Optimized geometrical parameters ($T=8.84$ a.u. and $R_{\text{wire}}=5.21$ a.u.) were used for the GGA electronic structure calculations of the Au MW and Au(6,0) nanotube.

Structural relaxation of the Au(6,0) nanowire with spin-orbit coupling (SOC) effect included led to changes in the optimized geometrical parameters of less then 1%.

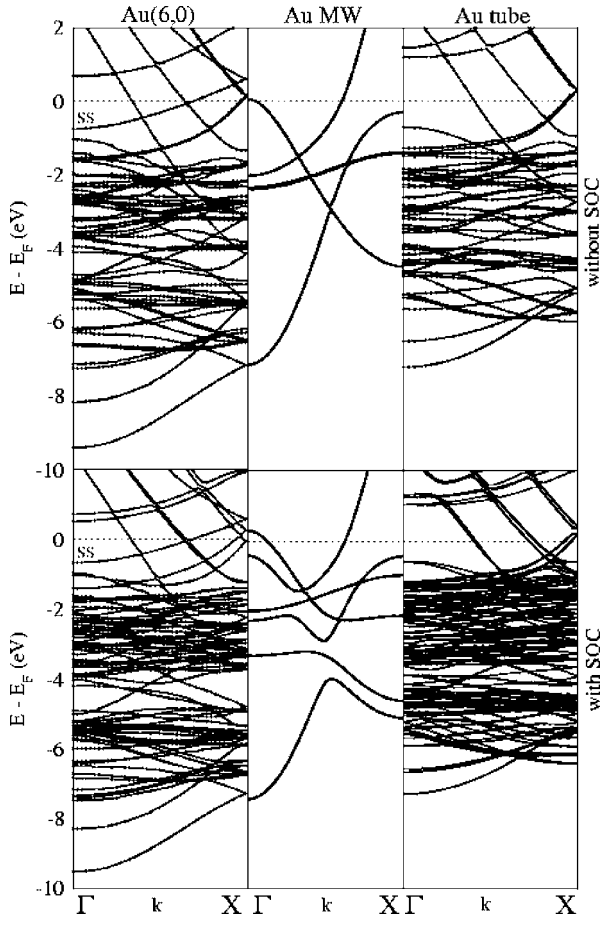

FIG. 3. Band structures of a Au(6,0) nanowire (left), a free Au MW (middle), and a Au(6,0) tube (right) for the atomic positions as calculated for the Au(6,0), $R_{\text{wire}}=5.21$ a.u., $T=8.84$ a.u. within the GGA, with (bottom panels) and without (top panels) spin-orbit coupling effects included. The band marked "ss" is discussed in the text.

3. Electronic structure

The GGA band structures for a Au(6,0) nanowire (left), a Au MW (middle), and a Au(6,0) tube (right) at the positions as in the Au(6,0) nanowire, are shown in Fig. 3. The top panel presents the band structures without SOC interaction included, the band structures with SOC effects included are shown in the bottom panel of Fig. 3. All the calculated structures show strong metallicity due to the s-bands of gold.

With "ss" in the band structures of the Au(6,0) nanowire we marked a surface state at the Γ-point below the Fermi energy. As one can conclude from the comparison between the band structures of the Au tube, Au MW, and Au nanowire, the appearance of this surface state is due to the hybridization of the states coming from the outer Au(6,0) nanotube and the inner Au MW. The charge density plots for this state are presented in Sec. III A 4.

The band structures for the Au(6,0) wire and Au(6,0) tube with SOC effects included [Fig. 3, bottom panel (left)] shows multiple band splittings as compared to the band structure without SOC, giving rise to a pronounced band splitting at the Fermi level. For the band structure of the Au(6,0) nano-

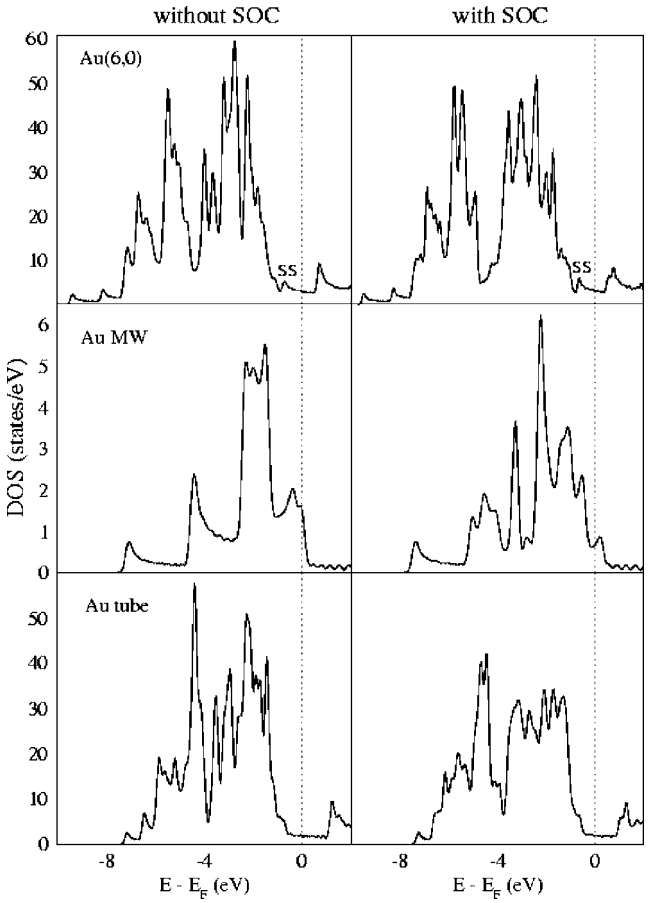

FIG. 4. Densities of states (DOS) of Au wires, calculated without (left panels) and with spin-orbit interaction (right panels). "ss" denotes the peak in the DOS coming from the energy band "ss" in Fig. 3 at the Γ-point. Top: DOS of the Au(6,0) nanowire. Middle: DOS of the free Au MW. Bottom: DOS of the Au(6,0) tube. DOS are calculated for the geometries discussed in the text.

wire calculated with and without spin-orbit interaction, the total number of conducting channels for ballistic transport is equal to six, which coincides with the number given in Ref. 5.

The band structure of the Au(6,0) nanowire (top left) coincides rather nicely with the band structure for this structure given in Ref. 5. The band structures of the Au MW are in good comparison to those in Refs. 24 and 39.

In the top of Fig. 4, the densities of states (DOS) of the Au(6,0) nanowire are shown, obtained with and without spin-orbit coupling. Including SOC, the figure shows an increase of the pseudogap between the two subgroups of *d*-bands, the first of them lying between −4 eV and −2 eV, while the other one is located in the energy interval between −7 eV to −5 eV. By "ss" we denote the peak in the DOS, which comes from the surface state "ss" in Fig. 3 at the Γ-point. The spin-orbit interaction changes also the DOS around the Fermi level, emphasizing this peak.

The total density of states for the gold monowire and the Au(6,0) tube, calculated with GGA at the positions as in the Au(6,0) nanowire with and without spin-orbit interaction, are shown at the bottom of Fig. 4. From the DOS we can observe, that due to the hybridization of the states coming from the outer Au tube and inner Au MW, the pseudogap between the two subgroups of *d*-bands is larger for the Au(6,0) nanowire, than for the Au(6,0) tube or Au MW. The same reason stands for the appearance of the surface state "ss" in the case of the Au(6,0) nanowire.

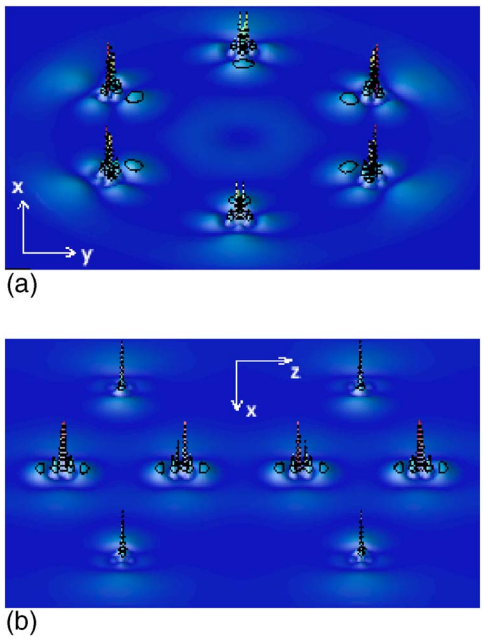

FIG. 5. (Color online) Charge density plots for the Au(6,0) wire for the energy band denoted by "ss" at the Γ-point in Fig. 3. Top: Charge density plot in *xy*-plane (perpendicular to the *z*-axis), cutting through the centers of the atoms in the outer hexagon ring. Bottom: Charge density plot in *xz*-plane, cutting through the centers of the inner strand atoms and 2 atoms in the outer shell hexagon ring.

4. Charge density

In Fig. 5 we present the charge density plots at the Γ-point for the energy band which is denoted by "ss" in Fig. 3. The charge density plot in the *xy*-plane (perpendicular to the *z*-axis), cutting through the centers of the gold atoms in one of the outer shell hexagons, is presented in the top panel of Fig. 5. The plot in the bottom panel shows the charge density in the *xz*-plane, cutting through the centers of the inner strand of gold atoms and two atoms in the outer hexagon of the gold wire. In Fig. 5 the surface state ("ss") character of the state at the outer atoms is clearly visible. For this state a d_{z^2} type orbital at the outer Au atoms is found with a slow decay into the vacuum. For inner strand atoms this state has p_z character.

The calculated work functions for the Au tube is 4.9 eV and 4.8 eV for the Au(6,0) nanowire, compared to the work function of the Au(111) surface of 5.31 eV.[40] The decrease of the work function can be addressed to the curvature effects.

B. Hybrid structure Fe@Au(6,0)

In analogy to the carbon based transition-metals hybrid structures which have been of the great theoretical and experimental interest during the last years,[15,21] one of the pro-

TABLE I. (Equilibrium) Fe-Fe distance, total spin magnetic moment in the unit cell μ_S^{tot} (per Fe atom), spin magnetic moment μ_S^{MT} in the MT sphere of Fe and magnetocrystalline anisotropy energy per Fe atom in three different types of Fe monowires and their dimers calculated with LDA and GGA. The Fe-Fe distance for the dimers is found by relaxation of the two Fe atoms in the double unit cell of the monomer. The magnetocrystalline anisotropy energy (MAE) is defined as the energy difference $\Delta E = E(\hat{e}_z) - E(\hat{e}_r)$ between the magnetization aligned along the wire axis and the radial direction of the wire. In the case of the hybrid structure Fe@Au(6,0) two possible in-plane alignments of the magnetization are possible: along the x and y axis. Corresponding MAEs are denoted by X and Y, respectively.

		Fe-Fe distance (a.u.)		μ_S^{tot} (μ_B)		μ_S^{MT} (μ_B)			MAE (meV/Fe atom)	
		LDA	GGA	LDA	GGA	LDA	GGA		LDA	GGA
Fe bare MW	monomer	4.14	4.28	3.25	3.32	2.92	3.01		1.4	5.5
	dimer	3.90	4.02	3.26	3.31	2.90	3.00		2.7	4.1
Fe@Au-MW	monomer	4.43	4.42	3.34	3.35	3.01	3.05		5.1	7.6
	dimer	3.92	4.10	3.31	3.30	2.97	3.03		8.9	7.3
Fe@Au(6,0)-MW	monomer	4.43	4.42	3.32	3.39	2.88	2.97	X	−32	−31
								Y	−32	−31
	dimer	4.14	4.20	3.28	3.37	2.86	2.96	X	−24	−26
								Y	−37	−34

posed routes towards spintronics applications of the metallic wires could be a combination of a metallic (nonmagnetic) tube and a nanowire inside, made of transition-metal atoms. A possible realization could be an Fe wire in a Au tube. Repeating the procedure known for growing Au tubes and wires,[33] but starting from FeAu alloys or an artificial FeAu layered superstructure, during the formation of the wire Au will segregate to the surface of the wire to lower the surface free energy which ultimately results in a Au covered Fe wire. To look into this problem in more details, we perform *ab initio* spin-polarized electronic structure calculations for the Fe@Au(6,0) hybrid structure.

1. Computational details

The calculations were carried out within the local density approximation using the functional of Vosko, Wilk, and Nusair[38] and within the generalized gradient approximation using the revPBE functional.[37] For self-consistency calculations of the hybrid structure we used 80 k-points in one half of the first Brillouin zone. For the gold and iron atoms the radii of MT spheres were chosen to be 2.0 a.u. Basis functions of all $\mathbf{G}$-vectors were included up to a length determined by the condition $|\mathbf{G}+k_z| < K_{\max}$ with $K_{\max}=3.6$ a.u.$^{-1}$. This corresponds to a vacuum angular expansion parameter for the basis functions of $m_{\max}=20$. For the plane-wave expansion of the charge density and potential a parameter $G_{\max}=3\cdot K_{\max}=10.8$ a.u.$^{-1}$ proved to give reliable results. The angular expansion of the vacuum charge density and potential was terminated at $m_{\max}=50$.

In order to investigate the magnetic structure of the hybrid system and the case of dimerization, we also performed a set of calculations on free-standing MWs of iron atoms, both within LDA (Ref. 38) and GGA.[37] For these calculations we used 64 k-points in one half of the first Brillouin zone. The parameters $G_{\max}$ and $K_{\max}$ were set to 11.4 a.u.$^{-1}$ and 3.8 a.u.$^{-1}$, respectively.

The results of the calculations on the hybrid structure Fe@Au(6,0) and the Fe MWs are summarized in Table I.

2. Geometrical structure

The geometrical structure of the system is shown in Fig. 2, having 12 gold atoms and 2 iron atoms per unit cell. It consists of the Au(6,0) outer tube and an inner strand of iron atoms, which replaces the inner monowire of gold atoms in the Au(6,0) nanowire. For the GGA calculations the period T of the structure and the radius of the outer shell of gold atoms were chosen to be the ones of the (6,0) gold nanowire optimized with GGA: 8.84 a.u. and 5.21 a.u., respectively. For the LDA calculations we use the optimal LDA values of 8.86 a.u. and 5.16 a.u. From total energy and force calculations we conclude that the inner Fe strand changes the geometrical parameters by less than 1%. As for the plain Au system, including the effects of the spin-orbit interaction did not cause any significant structural changes: the geometrical parameters changed by less then 1%, and the magnetic spin moment per iron atom changed by 0.5%.

We considered three different types of iron MWs: the bare MW, a MW with the interatomic Fe-Fe distance equal to that of the central strand of Au atoms in the Au(6,0) nanowire (denoted by Fe@Au-MW), and an iron monowire inside the Au(6,0) tube [Fe@Au(6,0)-MW]. For the free-standing MW the optimized Fe-Fe distance is 4.14 a.u. (LDA) and 4.28 a.u. (GGA), respectively, compared to 4.31 a.u. in Ref. 41 (GGA) and 4.26 a.u. in Ref. 23 (GGA).

Although we focus primarily on straight and linear monowires, we have observed that for the iron atoms inside the gold tube a zig-zag configuration appears to be energetically more favorable as compared to the unperturbed hybrid structure [as it was predicted for the free-standing iron MWs (Ref. 23)]. We concentrated our effort on considering the possibility of a Peierls dimerization of the Fe atoms along the chain. Thus, we double the unit cell with lattice constant a. Keeping the lattice constant fixed at $2a$, we investigate the total energy $E(\delta)$ as a function of the iron atom relaxation δ off the ideal high symmetry position along the chain axis. In most cases the dimerization was found to be preferable with a gain in total energy of around 30 meV resulting in changes

in the Fe-Fe distance due to dimerization in the range of $\delta = 5\%-12\%$ depending on the system (compared to 20 meV and 16% in Ref. 23). For more details see Table I.

The calculated work function for the Fe@Au(6,0) structure is 4.5 eV, which is 0.3 eV smaller than the work function of the Au(6,0) tube filled with the Au monowire.

3. Magnetic properties

In one-dimensional systems, the calculated magnetic moments of the iron atoms are much larger than the corresponding bulk value of 2.2 μ_B and the spin-polarization for the electrons at the Fermi level is quite large. The calculated hybrid structure has an average magnetic moment of around $2.92\mu_B$ per MT sphere of iron atom and $3.34\mu_B$ per Fe atom in the entire unit cell (cf. Table I). The magnetic moment of the gold atoms in all the calculations is around $0.02\mu_B$. For the iron MWs we found a magnetic moment of around $2.97\mu_B$ per MT sphere of iron atom and $3.30\mu_B$ per Fe atom in the entire unit cell (which is in a good comparison to the values in Refs. 23 and 41).

The decrease of the magnetic moment in the MT spheres of iron atoms in the hybrid structure comparing to the free-standing MWs gives the measure for the interaction between the iron atoms of the central strand and the atoms of the outer gold tube.

We checked the possibility of the structures to become antiferromagnetic (AFM). For the bare MW the ferromagnetic state (FM) is more favorable by 0.37 eV (LDA) and 0.33 eV (GGA) per Fe atom (similar values were obtained in Ref. 23). For the Fe@Au(6,0) structure this difference is 0.38 eV (LDA) per atom of iron and dimerization does not appear. We conclude that AFM solution is energetically very unfavorable and it is not considered any further.

The calculated orbital magnetic moments μ_L for the iron monowires lie in the range of $0.2–0.3\mu_B$ (similar values were obtained for the iron MWs in Ref. 42).

Magnetocrystalline anisotropy energies (MAE), being defined as energy differences $\Delta E = E(\hat{e}_z) - E(\hat{r}_x)$ between the magnetization aligned along the wire axis and the radial direction of the wire, were also calculated. For the hybrid structure Fe@Au(6,0) two possible in-plane alignments of the magnetization can lead to the stationary solutions: along the x and y axis. Corresponding MAEs, $\Delta E_X = E(\hat{e}_z) - E(\hat{e}_x)$ and $\Delta E_Y = E(\hat{e}_z) - E(\hat{e}_y)$, are denoted by X and Y in Table I. The coordinate system is chosen such that the x-axis points to the center of the gold atom in the outer hexagon ring and the y-axis points in between the two gold atoms in the hexagon ring. While in the case of free-standing MWs the magnetization is aligned along the wire axis with the MAEs between 1 meV to 7 meV, surprisingly in the case of the hybrid structure the situation changes drastically. The influence of the outer heavy gold atoms with an induced magnetic moment of just $0.02\mu_B$ per atom causes a change in the easy magnetization direction to in-plane along the x-axis. The further creation of the dimer changes the easy axis again to the y-axis. The average energy differences for the hybrid structure are around 30 meV per iron atom. In order to confirm the role of the encasing Au atoms on the magnetization direction, we carried out calculations where we switched off the spin-orbit interaction of the Au atoms by hand and we ended up at the results obtained for the single Fe wire: the easy axis of the magnetization is again along the wire, the hard axis is along the x direction, and the energy difference is 3.0 meV per iron atom (LDA) close to the value of 5.1 meV obtained for the single Fe wire (LDA). The shape anisotropy caused by the classical dipole interaction between the magnetic moments of the atoms prefers the in-chain direction as easy axis. The hard axis pointing radially from the wire is 0.1 meV higher in energy.

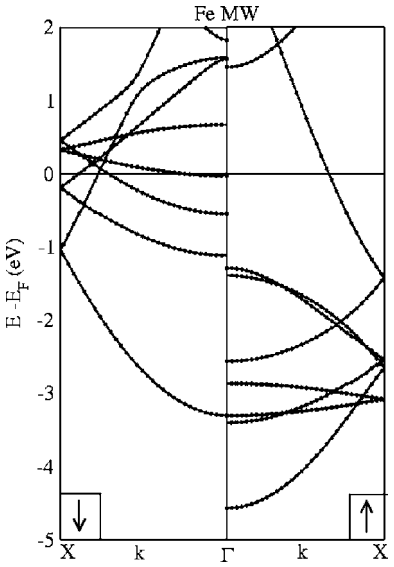

FIG. 6. Band structure of an Fe monowire with a lattice constant consistent with the gold tube for spin down and up channels (GGA). For minority spin, d-bands are concentrated around the Fermi level.

The magnetocrystalline anisotropy energy was calculated applying the force theorem.

4. Electronic structure

The band structure of the free-standing (6,0) gold tube calculated with GGA is shown in the right panel of Fig. 3. In Fig. 6 the backfolded GGA band structure of the free-standing iron monowire used to fill the gold tube is shown for spin up and spin down states (indicated by arrows). For this calculation the Fe-Fe distance in the monowire was kept to that of the gold monowire. It is clearly visible, that the minority d-states determine the electronic structure at the Fermi level. A profound symmetry analysis of the band structure and the charge density distribution for the Fe MW one can find in Ref. 43.

Figure 7 shows the atom-resolved band structure of the hybrid system, as calculated in GGA, reflecting the basic features of the iron monowire: most of the flat spin-down Fe d-bands are concentrated around the Fermi energy. From the plot of the total density of states (Fig. 8) we have obtained that the spin polarization at the Fermi level P_{E_F} reaches 74.3% (GGA), and 77.5% in the case of LDA. The spin-polarization P_{E_F} is defined as $(n_\downarrow(E_F) - n_\uparrow(E_F))/(n_\downarrow(E_F) + n_\uparrow(E_F))$, where $n_\downarrow(E_F)$ and $n_\uparrow(E_F)$ are total DOS for spin-down and spin-up channels at the Fermi level. Open (blue)

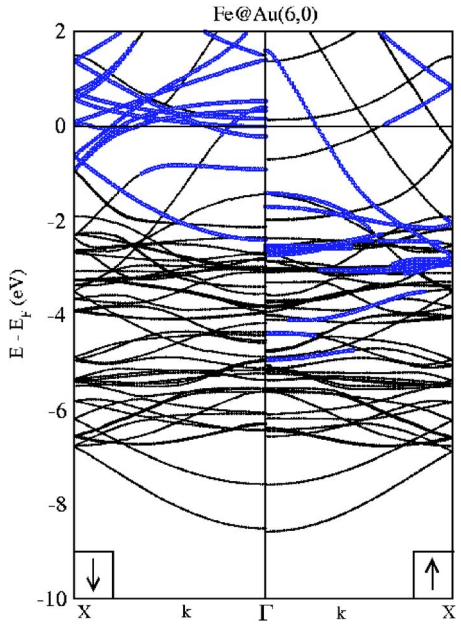

FIG. 7. (Color online) Band structure of the Fe@Au(6,0) system. Spin down and spin up are indicated by arrows. Open (blue) circles denote states located predominantly on iron atoms. It can be seen that narrow *d*-bands of Fe are responsible for large spin polarization at the Fermi level.

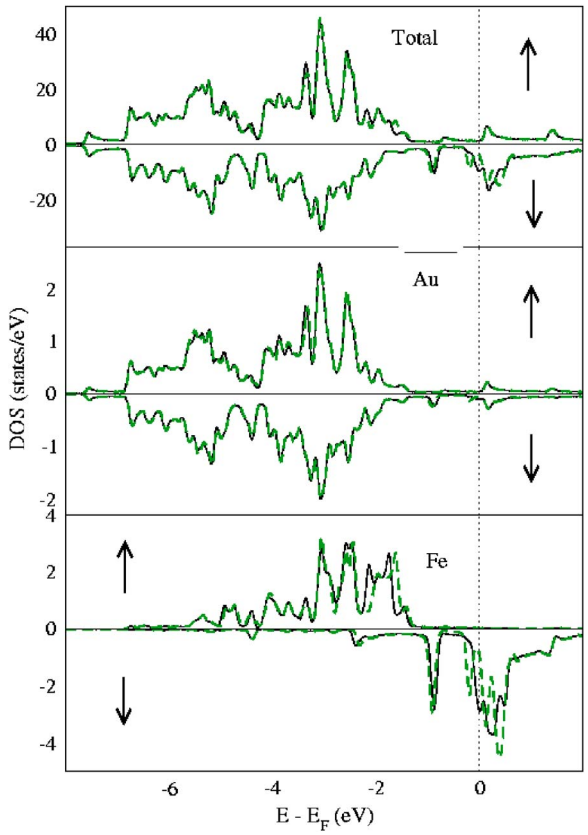

FIG. 8. (Color online) Densities of states (solid black lines) for Fe-filled (6,0) gold nanotube (spin up and down are indicated by arrows) and its dimer, calculated with GGA (corresponding DOS for the dimers are shown with dashed green lines). Top: total density of states. Middle: atom-resolved LDOS for the gold atoms. The Au LDOS is almost unaffected by the dimerization of the Fe strand. Bottom: atom-resolved DOS for the iron atoms. The large negative spin polarization is seen at the Fermi level.

circles in Fig. 7 indicate those states, which are predominantly localized on the iron sites. According to our definition this means, that the weight of a wave function in the Fe muffin-tins is three times larger than in the muffin-tins of Au atoms. The interstitial region is ignored. The atom-resolved band structure (Fig. 7) and atom-resolved local DOS (Fig. 8) clearly show that a large DOS at the Fermi level for the spin-down states comes from the *d*-states of iron. From the band structure and wave function analysis one can easily notice a large interaction of the iron states with the outer shell of gold for the spin-up channel: the hybridization of *s*- and *d*-states of iron and gold, located at the same energy interval, is significant.

In Fig. 9 the densities of states (GGA) for three different types of iron MWs (black solid lines) and their dimers (green dashed lines), are shown. In Fig. 9(c) we show again the atom-resolved LDOS of the iron atoms in the hybrid structure Fe@Au(6,0). Figure 8 represents the GGA densities of states for the hybrid structure (black solid lines) and its dimer (dashed green lines). Panels for spin down and up are marked with arrows. We conclude from Fig. 9(a) that the prominent peak of minority DOS at E_F is the dominant driving force for dimerization. Also in the Fe@Au(6,0) structure, a lowering of the DOS due to dimerization can be found [Fig. 8 (bottom)].

5. Charge density

In Fig. 10 we present the plots of the magnetization density at the Fermi energy $m_m^{E_F}(\mathbf{r})=\rho_\downarrow^{E_F}(\mathbf{r})-\rho_\uparrow^{E_F}(\mathbf{r})$, where $\rho_\downarrow^{E_F}(\mathbf{r})$ and $\rho_\uparrow^{E_F}(\mathbf{r})$ are the charge densities for the minority and majority spins around the Fermi level, respectively. Figure 10 (top) presents the magnetization density in the *xy*-plane, cutting through the centers of the gold atoms in an outer hexagon ring. Half of the hexagon is shown with the white lines connecting the gold atoms, as guide to the eyes. Figure 10 (bottom) shows the magnetization density in *xz*-plane, cutting through the centers of the iron atoms and one of the gold atoms in the outer shell hexagon. From these plots we see the domination of the *d*-bands of iron in the minority spin around the Fermi level. The magnetization density has a nonuniform distribution spilling out of the wire into the vacuum and should be, therefore, experimentally accessible, e.g. by the spin-polarized scanning tunneling microscopy (SP-STM). The magnetization density carries the signature of Au *p*-orbitals for the outer shell atoms and Fe *d*-orbitals for the inner atoms, signifying the hybridization of the minority Fe *d*-states with the Au *p*-states. Thus, the magnetization density at the Fermi energy is dominated by minority states.

The obtained results show that such hybrid structure as Fe@Au(6,0), if used for electron transport, will show a significant spin-polarization leading to strongly spin-polarized transport properties.

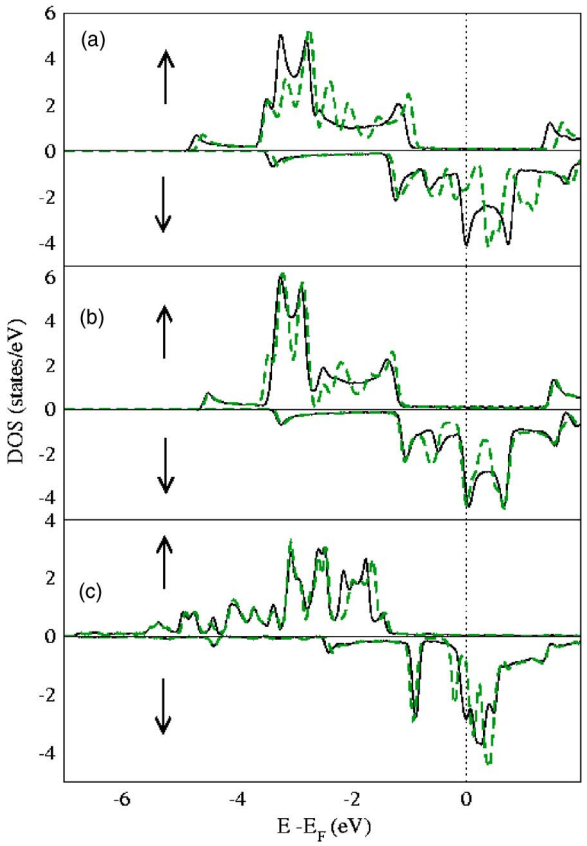

FIG. 9. (Color online) Densities of states for three different types of iron monowires and their dimers (spin up and down are indicated by arrows). DOS for the nondimerized MWs are shown with the solid (black) lines, DOS for the dimers are shown with the dashed (green) lines. (a) Total DOS for the bare MW and its dimer at the GGA interatomic distances of 4.28 a.u. and 4.02 a.u., respectively. (b) Total DOS of the bare Fe MW at the positions as in the Fe@Au(6,0) system and its dimer (GGA, 4.42 a.u. and 4.10 a.u., respectively). (c) Atom-resolved LDOS for the iron atoms inside the Fe@Au(6,0) hybrid structure and its dimer (GGA, 4.42 a.u. and 4.20 a.u., respectively).

IV. CONCLUSIONS

We reported on the implementation of the FLAPW method for first-principles calculations of truly one-dimensional systems. The implementation is realized as part of the FLEUR code. The method allows the calculation of electronic ground state properties and structural properties. The scheme includes the implementation of chiral cyclic symmetry group operations. It is an all-electron method applicable to all elements of the Periodic Table. The new program is particularly suitable for the study of magnetic properties (spin- and orbital moments, magnetic anisotropies, magnetic structures) of tubes and wires containing transition-metals or rare-earth metals.

We also investigated the hybrid structure Fe@Au(6,0) and the results show that this system has a large density of states around the Fermi level for minority electrons, exhibiting a large negative polarization at the Fermi energy. This makes this system interesting as a potential candidate for spin-dependent transport applications. The Au tube encasing the Fe wire changes the magnetization direction of the Fe wire from the direction along the wire to in-plane direction, and increases the magnetocrystalline anisotropy energy by an order of magnitude. The results on the plain Au(6,0) nanowire are in very good agreement with results of previous calculations.

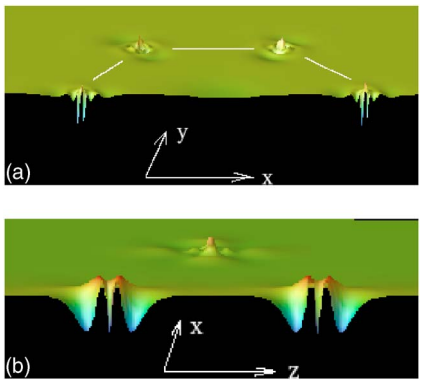

FIG. 10. (Color online) Spin-density plots for the Fe@Au(6,0) wire for the states around the Fermi energy. Top: Spin density plot in *xy*-plane (perpendicular to the tube axis), cutting through the centers of the atoms in the outer hexagon ring of gold. Bottom: Spin-density plot in *xz*-plane, cutting through the centers of the inner strand atoms of iron and one of the atoms of gold in the outer shell hexagon ring.

For a monowire, we have shown that the FLAPW method in the one-dimensional geometry is about two orders of magnitude faster than an equivalent calculation employing a bulk method in combination with a supercell approach. With this speed-up we feel prepared to investigate large one-dimensional multicomponent systems exhibiting complex magnetic interactions.

ACKNOWLEDGMENTS

We are grateful to Dr. E. E. Krasovskii and Dr. D. Wortmann for fruitful discussions and Dr. D. Wortmann for his assistance at the initial stage of this work.

APPENDIX A: EXPRESSIONS FOR THE BASIS FUNCTIONS AND CHARGE DENSITY IN THE VACUUM

The radial components of the basis functions in the vacuum, u, and their energy derivatives, $\dot{u}$, satisfy the following equations (for simplicity we omit the explicit dependence on r, m, G_z, and k_z):

$$\left[\frac{1}{r}\frac{d}{dr}\left(r\frac{d}{dr}\right)-\frac{m^2}{r^2}-(k_z+G_z)^2-V_0(r)+E_v\right]u=0, \tag{A1}$$

$$\left[\frac{1}{r}\frac{d}{dr}\left(r\frac{d}{dr}\right)-\frac{m^2}{r^2}-(k_z+G_z)^2-V_0(r)+E_v\right]\dot{u}=u, \tag{A2}$$

where E_v is a vacuum energy parameter, and $V_0(r)$ is the cylindrically symmetric $(m=0, G_z=0)$ component of the

vacuum potential. To ensure the uniqueness of the solutions, we also imply the following conditions:

$$\int_{R_{\mathrm{vac}}}^{\infty} r\,u^2(r)dr = 1, \tag{A3}$$

$$\int_{R_{\mathrm{vac}}}^{\infty} r\,u(r)\dot{u}(r)dr = 0. \tag{A4}$$

The A and B coefficients of the basis function in the vacuum region are found by matching the vacuum basis function at R_{vac} to the plane-waves in the interstitial region to guarantee that the basis function and its first radial derivative are continuous across the vacuum boundary. Thus they are found using a cylindrical expansion of the plane-wave:

$$e^{i\mathbf{G}_{\parallel}\mathbf{r}_{\parallel}}e^{i(G_z+k_z)z} = e^{i(k_z+G_z)z}\sum_m i^m e^{im(\varphi-\varphi_{\mathbf{G}_{\parallel}})}J_m(G_r r), \tag{A5}$$

where $\mathbf{G}_{\parallel}=(G_r,\varphi_{\mathbf{G}_{\parallel}})$ are expressed in polar coordinates, and J_m is a cylindrical Bessel function of the order m. Then the A and B coefficients are expressed as

$$A_m^{\mathbf{G}}(k_z) = i^m e^{-im\varphi_{\mathbf{G}_{\parallel}}} \times \frac{\dot{u}_m'(R_{\mathrm{vac}})J_m(G_rR_{\mathrm{vac}}) - \dot{u}_m(R_{\mathrm{vac}})G_rJ_m'(G_rR_{\mathrm{vac}})}{u_m(R_{\mathrm{vac}})\dot{u}_m'(R_{\mathrm{vac}}) - \dot{u}_m(R_{\mathrm{vac}})u_m'(R_{\mathrm{vac}})}, \tag{A6}$$

$$B_m^{\mathbf{G}}(k_z) = i^m e^{-im\varphi_{\mathbf{G}_{\parallel}}} \times \frac{u_m(R_{\mathrm{vac}})G_rJ_m'(G_rR_{\mathrm{vac}}) - u_m'(R_{\mathrm{vac}})J_m(G_rR_{\mathrm{vac}})}{u_m(R_{\mathrm{vac}})\dot{u}_m'(R_{\mathrm{vac}}) - \dot{u}_m(R_{\mathrm{vac}})u_m'(R_{\mathrm{vac}})}, \tag{A7}$$

where $u,\dot{u}$ as well as their radial derivatives u' and $\dot{u}'$ depend on G_z and k_z.

To express the charge density in the vacuum region in terms of A,B coefficients and radial basis functions, we first rewrite the wave function in the vacuum $\Psi_{k_z}^{\nu}(\mathbf{r})$ via the vacuum basis functions [Eq. (2)], and then substitute it into the expression for the charge density given by Eq. (12). This reads

$$\begin{aligned}\rho(\mathbf{r}) = \sum_{k_z,\nu} w(\nu,k_z) \sum_{\mathbf{G}',\mathbf{G}''} \sum_{m',m''} & e^{i(G_z'-G_z'')z} \\ & \times e^{i(m'-m'')\varphi}\left(c_\nu^{\mathbf{G}''}(k_z)\right)^* c_\nu^{\mathbf{G}'}(k_z) \\ & \times \left(A_m^{\mathbf{G}'}(k_z)u_{G_z',m}(k_z,r) + B_m^{\mathbf{G}'}(k_z)\dot{u}_{G_z',m}(k_z,r)\right) \\ & \times \left(A_m^{\mathbf{G}''}(k_z)u_{G_z'',m}(k_z,r) + B_m^{\mathbf{G}''}(k_z)\dot{u}_{G_z'',m}(k_z,r)\right)^*,\end{aligned} \tag{A8}$$

where $w(\nu,k_z)$ stands for $\omega(k_z)f(\nu,k_z)$ [Eq. (12)]. Taking into account that the radial basis functions do not depend on the $\mathbf{G}_{\parallel}$-component of the reciprocal lattice vector $\mathbf{G}$, we can contract the A and B coefficients in the following way:

$$A_m^{G_z}(k_z) = \sum_{\nu}\sum_{\mathbf{G}_{\parallel}} w(\nu,k_z)c_\nu^{G_z,\mathbf{G}_{\parallel}}(k_z)A_m^{G_z,\mathbf{G}_{\parallel}}(k_z),$$

$$B_m^{G_z}(k_z) = \sum_{\nu}\sum_{\mathbf{G}_{\parallel}} w(\nu,k_z)c_\nu^{G_z,\mathbf{G}_{\parallel}}(k_z)B_m^{G_z,\mathbf{G}_{\parallel}}(k_z). \tag{A9}$$

Extracting the $\mu=(m,G_z)$-components [Eq. (7)] of the vacuum charge density, given by Eq. (A8) and using the definition (A9) we arrive at the final expression:

$$\begin{aligned}\rho_{m,G_z}(r) = \sum_{k_z}\sum_{G_z'}\sum_{m'} \Big[& \left(A_{m'}^{G_z'}\right)^* A_{m+m'}^{G_z+G_z'}u_{G_z',m'}(r)u_{G_z+G_z',m+m'}(r) \\ & + \left(A_{m'}^{G_z'}\right)^* B_{m+m'}^{G_z+G_z'}u_{G_z',m'}(r)\dot{u}_{G_z+G_z',m+m'}(r) \\ & + \left(B_{m'}^{G_z'}\right)^* A_{m+m'}^{G_z+G_z'}\dot{u}_{G_z',m'}(r)u_{G_z+G_z',m+m'}(r) \\ & + \left(B_{m'}^{G_z'}\right)^* B_{m+m'}^{G_z+G_z'}\dot{u}_{G_z',m'}(r)\dot{u}_{G_z+G_z',m+m'}(r)\Big],\end{aligned} \tag{A10}$$

remembering that the A,B coefficients and the $u,\dot{u}$ functions depend also on k_z.

APPENDIX B: HAMILTONIAN AND OVERLAP MATRIX COEFFICIENTS IN THE VACUUM

As the space in a unit cell is partitioned into three different regions, the Hamiltonian and overlap matrix elements for the different regions can be calculated independently. The Hamiltonian and overlap matrix elements in the spheres and interstitial region can be found in Ref. 44, with slight modifications originating from the changes in the shape of the interstitial region, which is different to the film model. The contribution to the matrix elements of the overlap matrix due to the vacuum region are

$$\begin{aligned}S_{\mathrm{vac}}^{\mathbf{G}'\mathbf{G}}(k_z) = \sum_m \big[& (A_m^{\mathbf{G}'}(k_z))^* A_m^{\mathbf{G}}(k_z) + (B_m^{\mathbf{G}'}(k_z))^* B_m^{\mathbf{G}}(k_z) \\ & \times \langle \dot{u}_{G_z',m}(k_z)|\dot{u}_{G_z,m}(k_z)\rangle\big]\delta_{G_z',G_z}.\end{aligned} \tag{B1}$$

Expressions for the Hamiltonian matrix elements due to the vacuum region are more involved:

$$\begin{aligned}H_{\mathrm{vac}}^{\mathbf{G}'\mathbf{G}}(k_z) = \sum_{m',m} \big[& (A_{m'}^{\mathbf{G}'}(k_z))^* A_m^{\mathbf{G}}(k_z) t_{G_z,G_z'}^{uu,mm'}(k_z) \\ & + (A_{m'}^{\mathbf{G}'}(k_z))^* B_m^{\mathbf{G}}(k_z) t_{G_z,G_z'}^{u\dot{u},mm'}(k_z) \\ & + (B_{m'}^{\mathbf{G}'}(k_z))^* A_m^{\mathbf{G}}(k_z) t_{G_z,G_z'}^{\dot{u}u,mm'}(k_z) \\ & + (B_{m'}^{\mathbf{G}'}(k_z))^* B_m^{\mathbf{G}}(k_z) t_{G_z,G_z'}^{\dot{u}\dot{u},mm'}(k_z)\big],\end{aligned} \tag{B2}$$

where the elements of the t-matrix are given by the following expressions:

$$t_{G_z,G_z'}^{uu,mm'}(k_z) = I_{G_z,G_z',G_z'-G_z}^{uu,mm'(m'-m)}(k_z) + \delta_{m,m'}\delta_{G_z,G_z'}E_v,$$

$$t_{G_z,G_z'}^{u\dot{u},mm'}(k_z) = I_{G_z,G_z',G_z'-G_z}^{u\dot{u},mm'(m'-m)}(k_z) + \delta_{m,m'}\delta_{G_z,G_z'},$$

$$t^{\dot{u}u,mm'}_{G_z,G'_z}(k_z) = I^{\dot{u}u,mm'(m'-m)}_{G_z,G'_z,G'_z-G_z}(k_z),$$

$$t^{\dot{u}\dot{u},mm'}_{G_z,G'_z}(k_z) = I^{\dot{u}\dot{u},mm'(m'-m)}_{G_z,G'_z,G'_z-G_z}(k_z) + \delta_{m,m'}\delta_{G_z,G'_z}E_v\langle \dot{u}_{G'_z,m'}(k_z)|\dot{u}_{G_z,m}(k_z)\rangle. \tag{B3}$$

The I-terms above are given by

$$I^{\zeta\eta,mm'm''}_{G_z,G'_z,G''_z}(k_z) = I^{\eta\zeta,mm'm''}_{G_z,G'_z,G''_z}(k_z) = \int_{R_{\mathrm{vac}}}^{\infty} r\zeta_{G_z,m}(k_z,r)\,\eta_{G'_z,m'}(k_z,r)V_{m'',G''_z}(r)dr, \tag{B4}$$

where V_{m,G_z} are the radial components of the vacuum potential, ζ and η read for u or $\dot{u}$. As can be realized by inspection, the double summation over m,m' for each $\mathbf{G},\mathbf{G}'$ makes the setup of the Hamiltonian matrix elements for the vacuum as given in the present form rather time consuming. Among all vacuum contributions to the various parts of the method this is certainly the most time consuming contribution. A significant speedup is achieved using the following two facts: first, the elements of the t-matrix depend only on m, m', G_z, and G'_z, but not on $\mathbf{G}_\parallel$ and $\mathbf{G}'_\parallel$. Using this fact allows us to realize the following rather fast, contraction of the A and B coefficients

$$\tilde{A}^{\mathbf{G}'}_{m,G_z}(k_z) = \sum_{m'}(A^{\mathbf{G}'}_{m'}(k_z))^*(t^{uu,mm'}_{G_z,G'_z}(k_z) + t^{u\dot{u},mm'}_{G_z,G'_z}(k_z)),$$

$$\tilde{B}^{\mathbf{G}'}_{m,G_z}(k_z) = \sum_{m'}(B^{\mathbf{G}'}_{m'}(k_z))^*(t^{\dot{u}u,mm'}_{G_z,G'_z}(k_z) + t^{\dot{u}\dot{u},mm'}_{G_z,G'_z}(k_z)), \tag{B5}$$

to reduce the double summation by m,m' in Eq. (B2) to a single summation by m,

$$H^{\mathbf{G}'\mathbf{G}}_{\mathrm{vac}}(k_z) = \sum_m(\tilde{A}^{\mathbf{G}'}_{m,G_z}\cdot A^{\mathbf{G}}_m + \tilde{B}^{\mathbf{G}'}_{m,G_z}\cdot B^{\mathbf{G}}_m)(k_z). \tag{B6}$$

A second speed-up can be realized by exploiting the symmetry considerations. Knowing which particular $(m'',G''_z)=(m'-m,G'_z-G_z)$ components of the potential are forbidden by the symmetry of the system, we skip the summation over the corresponding (m,m',G_z,G'_z) elements in Eq. (B5), This makes the A and B coefficients contraction part negligible in computational time. The achieved speed-up due to the latter two considerations is here approximately $m_{\max}/2$, which for the calculations presented in the current paper, for the gold tube, for instance, gives a factor of 25.

Another consideration can be made based on the fact, that for large m the A and B coefficients decay very rapidly together with the t-matrix elements. This allows us to put the nondiagonal (m,m') part of the t-matrix to zero for $\{|m|,|m'|\}\leq m_{\mathrm{cutoff}}$, reducing therefore the m and m' summations in the construction of the Hamiltonian matrix. The actual value of the parameter m_{cutoff} should be determined such that it does not change the calculated properties in the range of the required numerical accuracy. For instance, for the gold monowire calculations, carried out with the angular basis functions expansion parameter $m_{\max}$ of 20, the choice $m_{\mathrm{cutoff}}=10$ proved to give a negligible difference (0.01%) in total energy differences, eigenvalues and Fermi energies compared to the case of $m_{\mathrm{cutoff}}=m_{\max}$.

APPENDIX C: GRADIENTS OF THE CHARGE DENSITY IN THE VACUUM FOR GGA CALCULATIONS

In the case of GGA, the exchange-correlation energy is written like

$$E_{\mathrm{xc}}[\rho] = \int \varepsilon_{\mathrm{xc}}(\rho(\mathbf{r}),|\nabla\rho(\mathbf{r})|)d\mathbf{r}, \tag{C1}$$

which defines the exchange-correlation potential as the functional derivative of E_{xc} with respect to the density ρ, i.e.,

$$V_{\mathrm{xc}}(\mathbf{r}) = \frac{\delta E_{\mathrm{xc}}[\rho]}{\delta\rho(\mathbf{r})} = \frac{\partial\varepsilon_{\mathrm{xc}}}{\partial\rho(\mathbf{r})} - \nabla\cdot\frac{\partial\varepsilon_{\mathrm{xc}}}{\partial\nabla\rho(\mathbf{r})}. \tag{C2}$$

Since the energy depends on $|\nabla\rho(\mathbf{r})|$, one finds from Eq. (C2) that in order to obtain V_{xc} not only $|\nabla\rho(\mathbf{r})|$, but also $\Delta\rho(\mathbf{r})$ and $\nabla\rho(\mathbf{r})\cdot\nabla|\nabla\rho(\mathbf{r})|$ are required.[45] The exchange-correlation energy and potential are found in the vacuum region on the real space cylindrical grid with the coordinates (r,φ,z). If we denote by $\hat{e}_r$, $\hat{e}_z$, and $\hat{e}_\varphi$ the orthogonal basis vectors at a given point in the vacuum, then the gradient of the charge density will be written as

$$\nabla\rho(\mathbf{r}) = \frac{\partial\rho(\mathbf{r})}{\partial r}\hat{e}_r + \frac{1}{r}\frac{\partial\rho(\mathbf{r})}{\partial\varphi}\hat{e}_\varphi + \frac{\partial\rho(\mathbf{r})}{\partial z}\hat{e}_z. \tag{C3}$$

The following two expressions stand for the absolute value of the gradient and the Laplacian:

$$|\nabla\rho(\mathbf{r})| = \sqrt{\left(\frac{\partial\rho(\mathbf{r})}{\partial r}\right)^2 + \frac{1}{r^2}\left(\frac{\partial\rho(\mathbf{r})}{\partial\varphi}\right)^2 + \left(\frac{\partial\rho(\mathbf{r})}{\partial z}\right)^2},$$

$$\Delta\rho(\mathbf{r}) = \frac{1}{r}\frac{\partial}{\partial r}\left(r\frac{\partial\rho(\mathbf{r})}{\partial r}\right) + \frac{1}{r^2}\frac{\partial^2\rho(\mathbf{r})}{\partial\varphi^2} + \frac{\partial^2\rho(\mathbf{r})}{\partial z^2}. \tag{C4}$$

These quantities and a subsequent expression $\nabla\rho(\mathbf{r})\cdot\nabla|\nabla\rho(\mathbf{r})|$, involve the partial derivatives of the first and second order of the charge density with respect to the spatial coordinates. The radial derivatives of the vacuum charge density components $\partial\rho_{m,G_z}(r)/\partial r$ and $\partial^2\rho_{m,G_z}(r)/\partial r^2$ are found numerically on the linear radial grid. Knowing the analytical dependence of the charge density in the vacuum on cylindrical φ and z coordinates, the mixed derivatives can thus be analytically found. For instance,

$$\frac{\partial^2\rho(\mathbf{r})}{\partial\varphi\,\partial r} = -i\sum_{G_z,m} m\frac{\partial\rho_{G_z,m}(r)}{\partial r}e^{im\varphi}e^{iG_zz}. \tag{C5}$$

The summations over G_z and m are carried out for every radial grid point r_i by means of two-dimensional Fourier transformations, obtaining the values of the densities on a uniform real space (φ, z) grid, as discussed in Sec. II C. Finally, the GGA exchange-correlation potential and energy density ε_{xc} are determined on the real space grid making an explicit use of analytical expansions for v_{xc} and ε_{xc}.

*Electronic address: y.mokrousov@fz-juelich.de

[1] S. Ijima, Nature (London) **354**, 56 (1991).
[2] A. Morales and C. Lieber, Science **279**, 208 (1998).
[3] K. Kondo and K. Takayanagi, Science **289**, 606 (2000).
[4] O. Gülseren, F. Ercolessi, and E. Tosatti, Phys. Rev. Lett. **80**, 3775 (1998).
[5] E. Tosatti, S. Prestepino, S. Kostlmeier, A. D. Corso, and F. D. D. Tolla, Science **291**, 288 (2001).
[6] K. Tsukagoshi, B. W. Alphenaar, and H. Ago, Nature (London) **401**, 1744 (1999).
[7] S. J. Tans, A. R. M. Verschueren, and C. Dekker, Nature (London) **393**, 49 (1998).
[8] R. Martel, T. Schmidt, H. R. Shea, T. Hertel, and P. Avouris, Appl. Phys. Lett. **73**, 2447 (1998).
[9] S. Heinze, M. Radosavljević, J. Tersoff, and P. Avouris, Phys. Rev. B **68**, 235418 (2003).
[10] J. Goldberger, R. He, Y. Zhang, S. Lee, H. Yan, H.-J. Choi, and P. Yang, Nature (London) **422**, 599 (2003).
[11] E. Hernández, C. Goze, P. Bernier, and A. Rubio, Phys. Rev. Lett. **80**, 4502 (1998).
[12] T. Kasuga, M. Hiramatsu, A. Hoson, T. Sekino, and K. Niihara, Adv. Mater. (Weinheim, Ger.) **11**, 1307 (1999).
[13] L. Krusin-Elbaum, D. Newns, H. Zeng, V. Derycke, J. Sun, and R. Sandstrom, Nature (London) **431**, 672 (2004).
[14] M. S. Dresselhaus, G. Dresselhaus, and P. Avouris, *Carbon Nanotubes* (Springer, Berlin, 2001).
[15] M. Monthioux, Carbon **40**, 1809 (2002).
[16] C. Guerret-Picourt, Y. L. Bouar, A. Lolseau, and H. Pascard, Nature (London) **372**, 761 (1994).
[17] D. Golberg, F.-F. Xu, and Y. Bando, Appl. Phys. A: Mater. Sci. Process. **76**, 479 (2003).
[18] K. Miyajima, A. Nakajima, S. Yabushita, M. Knickelbein, and K. Kaya, J. Am. Chem. Soc. **126**, 13202 (2004).
[19] J. Miller and A. Epstein, Angew. Chem., Int. Ed. Engl. **33**, 385 (1994).
[20] S. Uryu, Phys. Rev. B **69**, 075402 (2004).
[21] C.-K. Yang, J. Zhao, and J. P. Lu, Phys. Rev. Lett. **90**, 257203 (2003).
[22] M. Springborg, J. Chem. Phys. **87**, 7125 (1987).
[23] D. Spišák and J. Hafner, Phys. Rev. B **65**, 235405 (2002).
[24] A. Delin and E. Tosatti, Phys. Rev. B **68**, 144434 (2003).
[25] A. Delin and E. Tosatti, J. Phys.: Condens. Matter **16**, 8061 (2004).
[26] O. K. Andersen, Phys. Rev. B **12**, 3060 (1975).
[27] H. Krakauer, M. Posternak, and A. J. Freeman, Phys. Rev. B **19**, 1706 (1979).
[28] E. Wimmer, H. Krakauer, M. Weinert, and A. J. Freeman, Phys. Rev. B **24**, 864 (1981).
[29] Y. Oshima, A. Onga, and K. Takayanagi, Phys. Rev. Lett. **91**, 205503 (2003).
[30] D. J. Singh, *Planewaves, Pseudopotentials and the LAPW Method* (Kluwer, Dordrecht, 1994).
[31] M. Weinert, J. Math. Phys. **22**, 2453 (1981).
[32] V. Rodrigues, T. Fuhrer, and D. Ugarte, Phys. Rev. Lett. **85**, 4124 (2000).
[33] Y. Oshima, H. Koizumi, K. Mouri, H. Hirayama, K. Takayanagi, and Y. Kondo, Phys. Rev. B **65**, 121401(R) (2002).
[34] R. H. M. Smit, C. Untiedt, A. I. Yanson, and J. M. van Ruitenbeek, Phys. Rev. Lett. **87**, 266102 (2001).
[35] H. Ohnishi, Y. Kondo, and K. Takayanagi, Nature (London) **395**, 780 (1998).
[36] A. Delin, E. Tosatti, and R. Weht, Phys. Rev. Lett. **92**, 057201 (2004).
[37] Y. Zhang and W. Yang, Phys. Rev. Lett. **80**, 890 (1998).
[38] S. H. Vosko, L. Wilk, and M. Nussair, Can. J. Phys. **58**, 1200 (1980).
[39] L. D. Maria and M. Springborg, Chem. Phys. Lett. **323**, 293 (2000).
[40] N. V. Smith, C. T. Chen, and M. Weinert, Phys. Rev. B **40**, 7565 (1989).
[41] T. Nautiyal, T. H. Rho, and K. S. Kim, Phys. Rev. B **69**, 193404 (2004).
[42] C. Ederer, M. Komelj, and M. Fähnle, Phys. Rev. B **68**, 052402 (2003).
[43] M. Weinert and A. J. Freeman, J. Magn. Magn. Mater. **38**, 23 (1983).
[44] P. Kurz, Ph.D. thesis, RWTH-Aachen (2000).
[45] J. A. White and D. M. Bird, Phys. Rev. B **50**, R4954 (1994).